nature materials

LETTERS

https://doi.org/10.1038/s41563-022-01261-x

Solid–liquid–gas reaction accelerated by gas molecule tunnelling-like effect

Wen Wang[1,2,10,11], Tao Xu[1,11], Jige Chen[3,4,11], Junyi Shangguan[2,5], Hui Dong[6], Huishu Ma[4], Qiubo Zhang[2], Junwei Yang[7], Tingting Bai[8], Zhirui Guo[8], Haiping Fang[9] ✉, Haimei Zheng[2,5] ✉ and Litao Sun[1] ✉

Solid–liquid–gas reactions are ubiquitous and are encountered in both nature and industrial processes[1–4]. A comprehensive description of gas transport in liquid and following reactions at the solid–liquid–gas interface, which is substantial in regard to achieving enhanced triple-phase reactions, remains unavailable. Here, we report a real-time observation of the accelerated etching of gold nanorods with oxygen nanobubbles in aqueous hydrobromic acid using liquid-cell transmission electron microscopy. Our observations reveal that when an oxygen nanobubble is close to a nanorod below the critical distance (~1 nm), the local etching rate is significantly enhanced by over one order of magnitude. Molecular dynamics simulation results show that the strong attractive van der Waals interaction between the gold nanorod and oxygen molecules facilitates the transport of oxygen through the thin liquid layer to the gold surface and thus plays a crucial role in increasing the etching rate. This result sheds light on the rational design of solid–liquid–gas reactions for enhanced activities.

Solid–liquid–gas reactions can be found in hydrogen–oxygen fuel cell reactions, heterogeneous catalysis, metal corrosion in ambient environments and in a variety of other chemical reactions[1–7]. At solid–liquid–gas triple-phase interfaces, complex reactions occur in which many factors may play a role, including gas solubility and diffusion in liquids[8,9], ion or electron transfer across the interfaces[10] and so on[3,4]. Understanding, and further controlling, the local environment at the triple-phase interfaces are vital to controlling solid–liquid–gas reactions[1,4–6,9,11–13]. Gaseous reactants are often dissolved in the liquid phase and then diffuse to solid–liquid interfaces to participate in the reaction[4,8]. Recent ex situ studies have shown that, by delivering gases directly to the solid surface, the reaction rate could be significant increased by more than one order of magnitude[8,14], while it is also reported that a faster reaction can be realized when the gas bubble is close to the solid, separated only by a thin liquid membrane[15]. However, due to the absence of quantitative analysis of the reaction kinetics and an understanding of gas transport mechanism at the triple-phase interface, how the gas accelerates the reaction at the triple-phase interface remains unclear.

Herein we study the mechanisms of accelerated solid–liquid–gas reactions by taking advantage of recent advances in in situ transmission electron microscopy (TEM)[16–19]. The development of liquid-cell TEM, which can generate nanobubbles by radiolysis of liquids[15,20] and allow the direct imaging of dynamic reactions in liquids[21–26], presents an opportunity to visualize the critical pathways of triple-phase reactions at the nanoscale. We investigate the etching of gold (Au) nanorods in an aqueous solution in the presence of oxygen (O_2) gases as a model system of solid–liquid–gas reactions.

Gold, as a noble metal, is often considered inert. However, Au nanoparticles react with oxidative species such as O_2 dissolved in aqueous solution. For instance, single crystal Au nanorods can be etched completely in hydrogen bromide (HBr) solution at 70 °C in just a few minutes when bubbling air (Methods and Supplementary Figs. 1 and 2). Here, O_2 is the oxidizing agent and Br^- ions strongly coordinate with Au species, which notably decreases the electron potential of Au(I)/Au(0) to 0.959 V (versus the standard hydrogen eletcrode, SHE. Also see Supplementary Fig. 3). In this case, the reaction of Au nanocrystals with O_2 in the solution can be described thus[27]:

$$\mathrm{AuBr_2^-} + e^- \rightarrow \mathrm{Au} + 2\mathrm{Br}^- \quad E = 0.959\,V\,\text{versus SHE} \tag{1}$$

$$\mathrm{O_2} + 4\mathrm{H}^+ + 4e^- \rightarrow 2\mathrm{H_2O} \quad E = 1.299\,V\,\text{versus SHE} \tag{2}$$

Bubbling O_2 gases through the solution dramatically enhances etching of Au nanorods, as compared with the case with the solution open to still air (Supplementary Fig. 2).

We performed an in situ study of Au nanorod etching in HBr aqueous solution in the presence of O_2 gas using liquid-cell TEM. The reaction liquid was encapsulated between two carbon films supported on Cu frames (Methods and Fig. 1a). Radiolysis of aqueous hydrogen halide solution generates gas bubbles, including H_2, O_2 and halogens[28,29]. Halogen gases, such as Cl_2 and HCl, can split into Cl^- and H^+ to accelerate etching, but this was unlikely to have occurred in our in situ experimental system (Supplementary Fig. 3). Here, the initial gas product was expected to be dominated

---

[1]SEU-FEI Nano-Pico Center, Key Laboratory of MEMS of Ministry of Education, Collaborative Innovation Center for Micro/Nano Fabrication, Device and System, Southeast University, Nanjing, China. [2]Materials Sciences Division, Lawrence Berkeley National Laboratory, Berkeley, CA, USA. [3]Shanghai Synchrotron Radiation Facility, Zhangjiang Laboratory, Shanghai Advanced Research Institute, Chinese Academy of Sciences, Shanghai, China. [4]Shanghai Institute of Applied Physics, Chinese Academy of Sciences, Shanghai, China. [5]Department of Materials Science and Engineering, University of California, Berkeley, CA, USA. [6]Key Laboratory of Welding Robot and Application Technology of Hunan Province, Engineering Research Center of Complex Tracks Processing Technology and Equipment of Ministry of Education, Xiangtan University, Xiangtan, China. [7]School of Arts and Sciences, Shanghai Dianji University, Shanghai, China. [8]The Second Affiliated Hospital, Key Laboratory for Aging & Disease, Nanjing Medical University, Nanjing, China. [9]School of Physics and National Engineering Research Center of Industrial Wastewater Detoxication and Resource Recovery, East China University of Science and Technology, Shanghai, China. [10]Present address: School of Mechanics and Safety Engineering, Zhengzhou University, Zhengzhou, China. [11]These authors contributed equally: Wen Wang, Tao Xu, Jige Chen. ✉e-mail: fanghaiping@sinap.ac.cn; hmzheng@lbl.gov; slt@seu.edu.cn

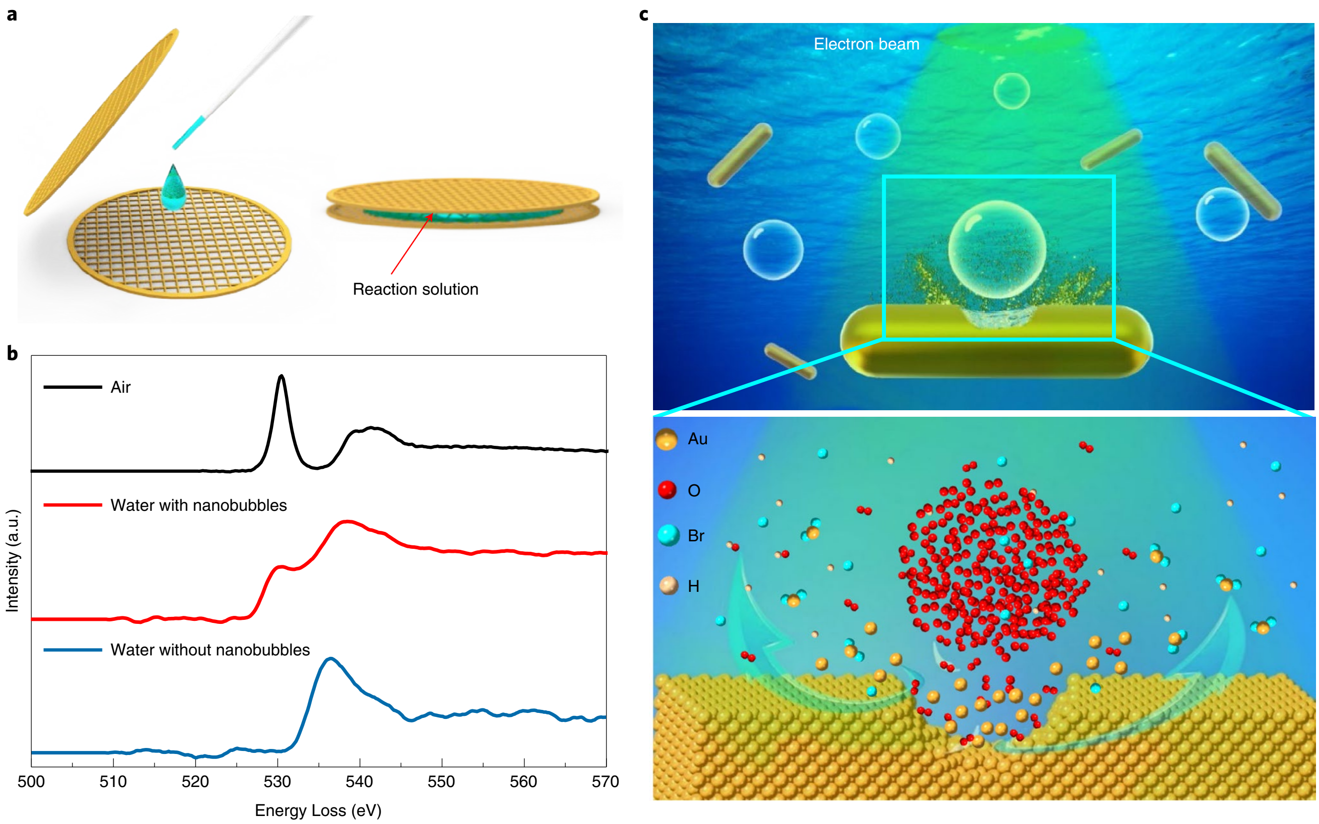

Fig. 1 | Schematic illumination of a solid–liquid–gas reaction established within a liquid cell. **a**, Schematic liquid cell encapsulating the reaction solution. **b**, EELS showing the O K-edge of air (black, reference spectrum from Gatan EELS Atlas), water without nanobubbles (blue) and water with nanobubbles generated by electrolysis of water at a later stage (red). The O K-edge of water with nanobubbles, showing evidence of molecular O_2 at ~527 eV as compared with the reference spectrum from O_2 gas (black). **c**, Schematic illustration of the etching of gold nanorods in HBr solution, with O_2 nanobubbles in the near distance. a.u., Arbitrary units.

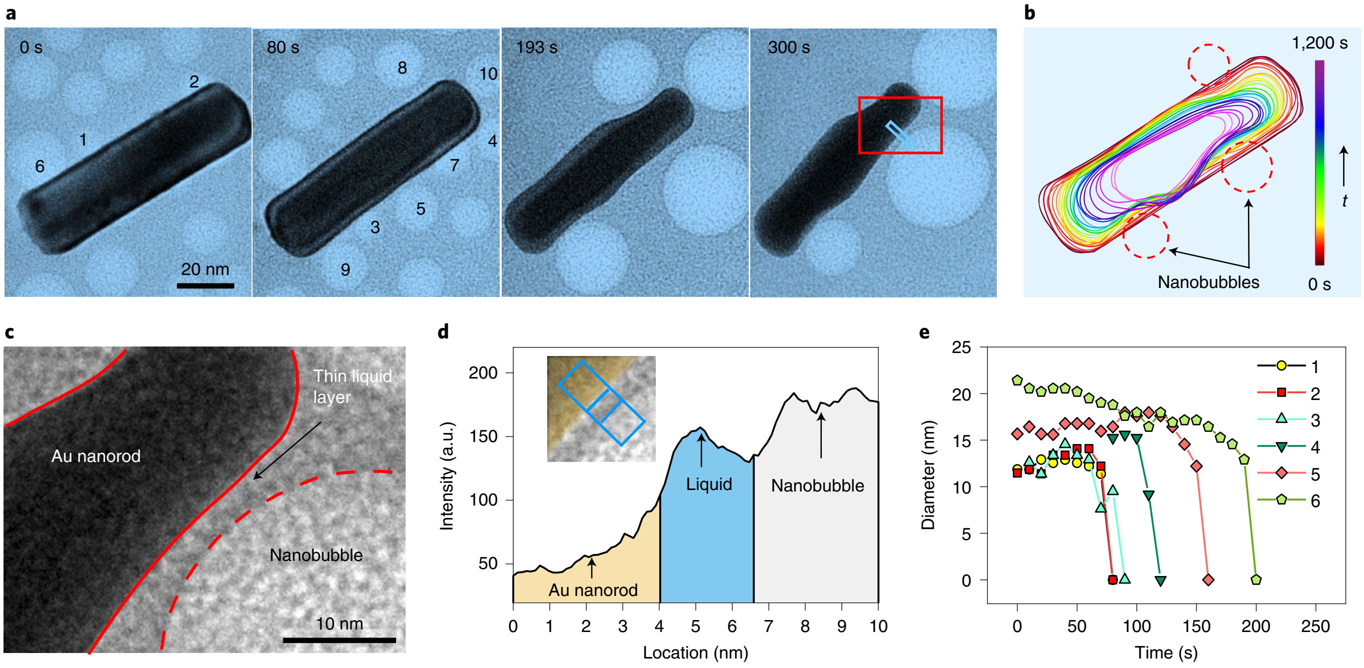

Fig. 2 | Real-time observation of Au nanorod etching process in the presence of O_2 gas nanobubbles in a liquid cell. **a**, Time-sequential TEM micrographs showing real-time shape evolution of the nanorod during etching; images are extracted from Supplementary Video 1. **b**, Corresponding contour map highlighting indents developed near nanobubbles. **c**, The enlarged image (red rectangle in **a**) clearly showing the thin liquid layer between the nanorod and nanobubble. **d**, Intensity profile of the selected area shown in **a**. **e**, Diameter changes in nanobubbles with time. Numbers represent the different nanobubbles marked in **a**.

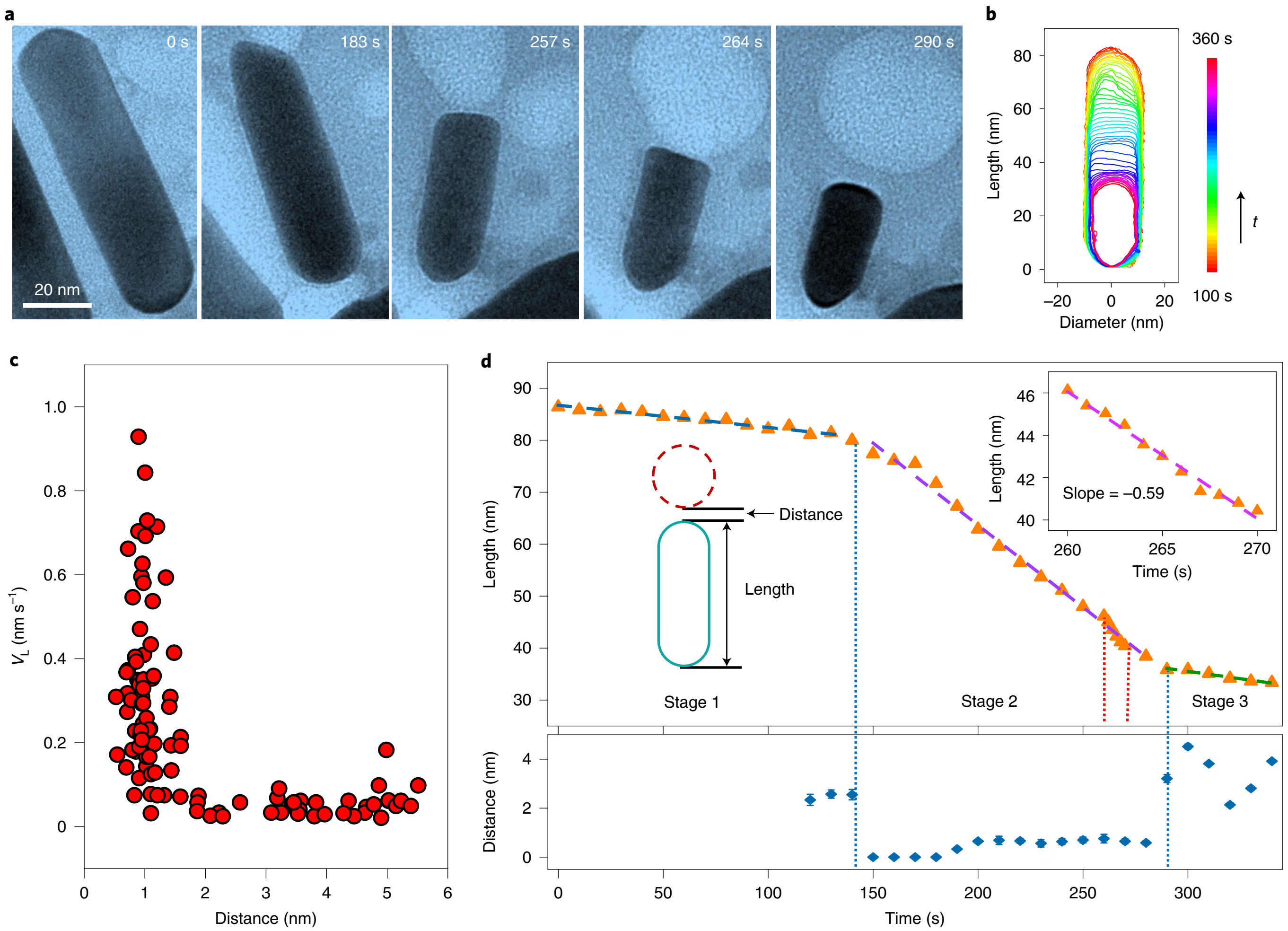

Fig. 3 | Real-time observation of Au nanorod etching with an O_2 gas nanobubble at the nanorod end. a, Sequential TEM images of the Au nanorod during etching. **b**, Time-labelled contours showing the shape evolution of the nanorod in **a**. **c**, Statistical plot showing longitudinal etching rate as a function of the distance between the nanobubble and nanorod surface. **d**, Top, changes in nanorod length as a function of time; bottom, corresponding distance between nanorod and nanobubble; inset, magnified view of the plot over 260–270 s with an average etching rate of 0.59 nm s^{-1}, which is one order of magnitude faster than that in stage 1. Especially at the 266 s time point, the etching rate reached 0.9 nm s^{-1}, which is 20 times higher than in stage 1.

by H_2: O_2 is produced at a later stage and in far lower amounts[30] (Methods). Electron energy loss spectroscopy (EELS) of the solution with gas nanobubbles confirms the presence of O_2 gas molecules within the nanobubbles (Fig. 1b and Methods). H_2 nanobubbles have been reported to act as a reservoir of reductant and do not contribute to the etching of Au[31], and we also observed in our system that most nanobubbles do not affect the etching of nanorods or reduce Au ions back to the metallic phase (Supplementary Fig. 4). Therefore, O_2 nanobubbles (at least those nanobubbles containing mostly O_2) can be distinguished by the enhanced etching of Au nanorods during in situ imaging.

It is noted that, besides O_2 nanobubbles, other oxidative species, such as H_2O_2, $OH^\bullet$ and $HO_2^\bullet$, can also be generated during electrolysis of H_2O. These oxidative species are considered to be uniformly distributed in water in the irradiated area, leading to a previously reported uniform etching of Au nanorod[22,32] (Supplementary Fig. 5 and Supplementary Video 1). Here, we focus on the impact of O_2 nanobubbles on the solid–liquid–gas reaction of Au nanorods (Fig. 1c).

Figure 2 shows the morphological evolution of a Au nanorod during etching, surrounded by several nanobubbles (Supplementary Video 2). The nanorod develops indents near the nanobubbles as etching proceeds (Fig. 2a,b). It is clear that materials at the indented areas are etched away rather than being redistributed to other parts of the nanorod (Supplementary Fig. 6). Etching of the Au nanorod in this scenario is drastically different from that without a gas nanobubble in the near distance, in which the Au nanorod shows a smooth surface of ellipsoidal shape during etching (Supplementary Fig. 5 and Supplementary Video 1). It is noted that a thin liquid layer between the nanobubble and nanorod can be identified while the indent is developing (Fig. 2c,d). The calculated ratio between O_2 molecules and water molecules near the nanobubble is about three orders of magnitude higher than for the oxygen saturated solution, which further indicates that the environment near the nanobubble should be treated as a gas–liquid–solid system rather than a solution with oxygen molecules. Therefore, etching at the indented areas results from solid–liquid–gas reactions, unlike the solid–liquid etching process shown in Supplementary Fig. 5.

We also note that most nanobubbles shrink and disappear eventually during etching (Fig. 2e), suggesting that nanobubbles participate in the reaction as a reactant rather than as a reaction product from unexpected side reactions. The growth of certain nanobubbles is attributed to Ostwald ripening between nanobubbles, which is highlighted separately in Supplementary Fig. 7. In addition to the likelihood of them being being consumed during the Au etching process, slow shrinking of nanobubbles may result

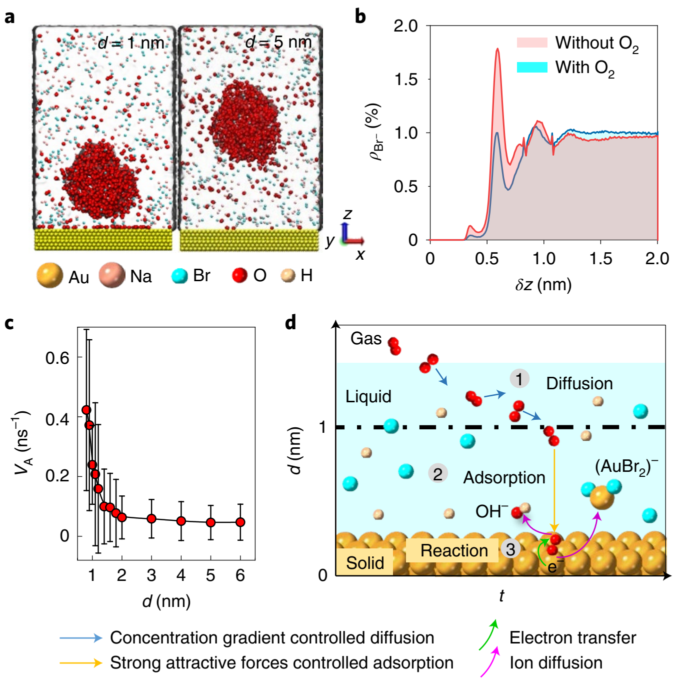

Fig. 4 | Involvement of O_2 gas in the Au nanorod etching pathway. **a**, Schematic of MD calculation model of O_2 molecules in a nanobubble, with distance $d=1$ nm (left) and 5 nm (right) from the Au nanorod surface, adsorbing on the nanorod surface at time $t=2$ ns. **b**, Distribution of Br^- ions as a function of distance to the nanorod surface with and without O_2 molecules. **c**, Adsorption rate of O_2 molecules, V_A, as a function of distance between the nanobubble and nanorod surface. Error bars, s.d. **d**, Schematic illustration of the Au nanorod etching pathway in the presence of O_2, including O_2 diffusion controlled by concentration gradient (1), adsorption of O_2 molecules by strongly attractive van der Waals interactions with Au atoms (2) and reaction on the nanorod surface (3).

from their instability due to other factors, such as increased local ion concentration[33].

To quantify enhanced etching of the Au nanorod by nanobubbles, we investigated etching of one with a nanobubble near one tip (Fig. 3a and Supplementary Video 3). The contour map highlights a much faster etching along the long axis compared with the diameter (Fig. 3b). Notably higher longitudinal etching rates, V_L, were observed when the distance to the nanobubble was ~1 nm or less (Fig. 3c). Measurement results from additional nanobubbles agree with this observed trend (Supplementary Figs. 8–11). Changes in nanorod length with time, and corresponding changes of the distance between the nanobubble and tip, are also plotted (Fig. 3d). Based on the values of V_L, which can be estimated by the slopes of linear fitting, three stages can be identified (stage 1, 0.043 nm s^{-1}; stage2, 0.31 nm s^{-1}; and stage 3, 0.056 nm s^{-1}).

In stage 1 a low etching rate is seen (0.043 nm s^{-1}) because there is no effective nanobubble close to the nanorod. As the nanobubble gradually approaches the nanorod (~1 nm, starting at 150 s), the etching rate increases significantly at an average of 0.31 nm s^{-1} (stage 2). Especially after two adjacent nanobubbles have merged, the average and highest etching rates are 0.59 and 0.9 nm s^{-1}, respectively, which are ten- and 20-fold higher than that in stage 1 (Fig. 3d, inset, and Supplementary Fig. 12). We note that the distance between the nanobubble and nanorod surface d is in a similar range between 260 and 270 s, suggesting that more highly reactive gas molecules enhance etching. In stage 3 the nanorod undergoes slow etching again when the nanobubble moves further away (after 290 s; also see Supplementary Fig. 12). It is interesting that accelerated etching disappears immediately the nanobubble leaves the nanorod surface (Fig. 3a,d, Supplementary Figs. 13 and 14 and Supplementary Videos 3 and 4), which is consistent with the rapid enhanced reaction when the nanobubble approaches within 1 nm, illustrating that the ultra-thin liquid layer between the solid and liquid is the key to accelerating the reaction rather than requiring direct contact of gas with the solid surface. It has been reported that nanorods always show more rapid etching at the tip than the sides, due to the lower coordination number and surface ligand density of the tip atoms[22,32]. To avoid the influence of nanorod geometry on etching rate, we compared the ratios of longitudinal and transverse etching rate (V_L/V_D) of different nanorods with and without nanobubbles. The results also confirmed enhanced etching by nanobubbles (Supplementary Fig. 15).

To uncover the mechanisms of accelerated etching by nanobubbles, we established a molecular dynamics (MD) simulation model of the adsorption process of O_2 molecules in an aqueous NaBr solution (Fig. 4a). The adsorption site of Br^- ions in its density distribution near the Au nanorod surface remained at $\delta z=0.6$ nm in the presence of O_2, suggesting that the accelerated etching of Au does not arise from local ion concentrations but, rather, the reaction between O_2 and nanorod (Fig. 4b). The adsorption rate of O_2 molecules, $V_A=1/<T_A>$, shows a much higher value at distances of ~1.0 nm or less and was drastically reduced at distances >1 nm (Fig. 4c). Here T_A represents the average adsorption time of O_2 on the Au nanorod surface. The calculated adsorption rates are thus in good agreement with the observed experimental results of etching rates shown in Fig. 3c. The high adsorption rate within 1.0 nm indicates the existence of strong attractive forces from the Au nanorod surface at close range. The adsorption process is governed by the slow diffusion of O_2 molecules at greater distances (>1.0 nm). Furthermore, ab initio molecular dynamics simulations show that the interaction energy of O_2 with the Au substrate is dependent on the distance between them, which is consistent with the observed trend of O_2 absorption rates as discussed above. In addition, we found that van der Waals interactions largely contributed to the attractive force in O_2 absorption (Supplementary Figs. 16 and 17).

Combining experimental results with MD simulations, we expect that two different O_2 transfer mechanisms participate in solid–liquid–gas reactions. When the distance between O_2 molecules and the nanorod surface is greater than a critical distance (~1 nm), slow O_2 molecule diffusion is expected. When the distance is reduced to less than the critical distance, O_2 molecules are easily adsorbed on the Au nanorod surface by the strongly attractive van der Waals interactions and more rapid etching is expected. The corresponding solid–liquid–gas etching pathway with different distances between nanorod and nanobubble is summarized in Fig. 4d.

It is expected that this mechanism can be extended to other solid–liquid–gas reaction systems. We used an electron beam to irradiate an HBr aqueous solution containing palladium (Pd) nanocubes and found that the edge of the Pd nanocube was concave when a nanobubble was seen nearby (Supplementary Fig. 18). Quantitative analysis shows that when the ultra-thin liquid layer between the nanocube and nanobubble is <1 nm, the average transverse etching rate of the nanocube can be increased by 2.5-fold.

It is known that the marine splash area is the most serious corrosion area of low-alloy steel in marine engineering, cavitation erosion can cause serious damage to a ship's propeller and it is also shown, in our ex situ experiment, that bubbling air can accelerate the etching rate of a Au nanorod in HBr solution. Therefore, the thickness of the liquid layer and the movement of nanobubbles will dramatically affect reaction rate. The identification of mechanisms for accelerated solid–liquid–gas reactions provides a future opportunity for the design and control of triple-phase complex reactions in industrial and material synthesis. Some parameters in the reaction condition should be considered carefully, including stirring rate, temperature, hydrophobicity of the material, ventilation mode and location, for these may change the likelihood of formation of an ultra-thin liquid layer and affect reaction rate. We also propose several promising strategies for acceleration of the triple-phase reaction, through specific ventilation approaches in different scenarios (Supplementary Fig. 19).

In summary, we captured the solid–liquid–gas etching process of an Au nanorod in real time at nanoscale using liquid-cell TEM. Different from the conventional view that a more rapid approach of nanobubbles toward the solid leads to a more rapid reaction, our investigation identifies two distinct reaction scenarios dependent on liquid layer thickness, which determine the gas transport mechanism. When the thickness of the liquid layer is reduced, with strong short-range attractive forces, oxygen molecules in the bubbles are directly adsorbed on the nanorod surface leading to a more rapid reaction rate. This study enhances our knowledge of the reaction pathway of the triple-phase boundary and provides a promising approach to modify the solid–liquid–gas reaction rate. Moreover, it shows that liquid-cell TEM provides an observational and mechanistic understanding of solid–liquid–gas reaction at relevant temporal and distance scales, which offers great potential for addressing many fundamental issues where nanoscale gas and liquid states are involved.

Online content

Any methods, additional references, Nature Research reporting summaries, source data, extended data, supplementary information, acknowledgements, peer review information; details of author contributions and competing interests; and statements of data and code availability are available at https://doi.org/10.1038/s41563-022-01261-x.

Received: 9 November 2020; Accepted: 19 April 2022;

References

1. Snyder, J., Fujita, T., Chen, M. W. & Erlebacher, J. Oxygen reduction in nanoporous metal-ionic liquid composite electrocatalysts. *Nat. Mater.* **9**, 904–907 (2010).
2. Irvine, J. T. S. et al. Evolution of the electrochemical interface in high-temperature fuel cells and electrolysers. *Nat. Energy* **1**, 15014 (2016).
3. Qiao, M. & Titirici, M.-M. Engineering the interface of carbon electrocatalysts at the triple point for enhanced oxygen reduction reaction. *Chem. Eur. J.* **24**, 18374–18384 (2018).
4. Tang, C., Wang, H.-F. & Zhang, Q. Multiscale principles to boost reactivity in gas-involving energy electrocatalysis. *Acc. Chem. Res.* **51**, 881–889 (2018).
5. Chen, P., Guo, M., Han, W., Wang, Z. & Wang, C. Study of corrosion evolution of carbon steel exposed to an industrial atmosphere. *Corros. Eng. Sci. Technol.* **54**, 241–248 (2019).
6. Bu, F. R., Li, J. N. & Huang, H. L. Effects of electrolyte thickness, chloride ion concentration, and an external direct current electric field on corrosion behaviour of silver under a thin electrolyte layer. *Corros. Eng. Sci. Technol.* **54**, 143–153 (2018).
7. Zhu, Y. P., Guo, C., Zheng, Y. & Qiao, S.-Z. Surface and interface engineering of noble-metal-free electrocatalysts for efficient energy conversion processes. *Acc. Chem. Res.* **50**, 915–923 (2017).
8. Li, J. et al. Breathing-mimicking electrocatalysis for oxygen evolution and reduction. *Joule* **3**, 557–569 (2019).
9. Liu, Z. et al. Superaerophilic carbon-nanotube-array electrode for high-performance oxygen reduction reaction. *Adv. Mater.* **28**, 7155–7161 (2016).
10. Seh, Z. W. et al. Combining theory and experiment in electrocatalysis: insights into materials design. *Science* **355**, eaad4998 (2017).
11. Liu, M., Zhao, Z., Duan, X. & Huang, Y. Nanoscale structure design for high-performance Pt-Based ORR catalysts. *Adv. Mater.* **31**, e1802234 (2019).
12. Qiao, M. et al. Oxygenophilic ionic liquids promote the oxygen reduction reaction in Pt-free carbon electrocatalysts. *Mater. Horiz.* **4**, 895–899 (2017).
13. Lu, Q. Highly porous non-precious bimetallic electrocatalysts for efficient hydrogen evolution. *Nat. Commun.* **6**, 6567 (2015).
14. Liu, Z., Sheng, X., Wang, D. & Feng, X. Efficient hydrogen peroxide generation utilizing photocatalytic oxygen reduction at a triphase interface. *iScience* **17**, 67–73 (2019).
15. Hutzler, A. et al. In situ liquid cell TEM studies on etching and growth mechanisms of gold nanoparticles at a solid-liquid-gas interface. *Adv. Mater. Interfaces* **6**, 1901027 (2019).
16. Sun, J. et al. Liquid-like pseudoelasticity of sub-10-nm crystalline silver particles. *Nat. Mater.* **13**, 1007–1012 (2014).
17. Zhou, Y. et al. In situ observation of atomic-scale stability limit of Cu nanoparticles. *Mater. Today Nano.* **4**, 32–37 (2018).
18. Xu, H. et al. Dynamic structure-properties characterization and manipulation in advanced nanodevices. *Mater. Today Nano* **7**, 100042 (2019).
19. Yang, J. et al. Formation of two-dimensional transition metal oxide nanosheets with nanoparticles as intermediates. *Nat. Mater.* **18**, 970–976 (2019).
20. Shin, D. et al. Growth dynamics and gas transport mechanism of nanobubbles in graphene liquid cells. *Nat. Commun.* **6**, 6068 (2015).
21. Zheng, H. et al. Observation of single colloidal platinum nanocrystal growth trajectories. *Science* **324**, 1309–1312 (2009).
22. Ye, X. et al. Single-particle mapping of nonequilibrium nanocrystal transformations. *Science* **354**, 874–877 (2016).
23. Zhu, C. et al. In-situ liquid cell transmission electron microscopy investigation on oriented attachment of gold nanoparticles. *Nat. Commun.* **9**, 421 (2018).
24. Ou, Z., Wang, Z., Luo, B., Luijten, E. & Chen, Q. Kinetic pathways of crystallization at the nanoscale. *Nat. Mater.* **19**, 450–455 (2020).
25. Paul, J. M. et al. Calcium carbonate nucleation driven by ion binding in a biomimetic matrix revealed by in situ electron microscopy. *Nat. Mater.* **14**, 394–399 (2015).
26. Xu, T. & Sun, L. Investigation on material behavior in liquid by in situ TEM. *Superlattices Microstruct.* **99**, 24–34 (2016).
27. Tsung, C.-K. et al. Selective shortening of single-crystalline gold nanorods by mild oxidation. *J. Am. Chem. Soc.* **128**, 5352–5353 (2006).
28. Jian, Y. et al. In situ study of oxidative etching of palladium nanocrystals by liquid cell electron microscopy. *Nano Lett.* **14**, 3761–3765 (2014).
29. Woehl, T. J. & Abellan, P. Defining the radiation chemistry during liquid cell electron microscopy to enable visualization of nanomaterial growth and degradation dynamics. *J. Microsc.* **265**, 135–147 (2017).
30. Schneider, N. M. et al. Electron-water interactions and implications for liquid cell electron microscopy. *J. Phys. Chem. C Nanomater. Interfaces* **118**, 22373–22382 (2014).
31. Hauwiller, M. R. et al. Gold nanocrystal etching as a means of probing the dynamic chemical environment in graphene liquid cell electron microscopy. *J. Am. Chem. Soc.* **141**, 4428–4437 (2019).
32. Wang, W. et al. Controlled oxidative etching of gold nanorods revealed through in-situ liquid cell electron microscopy. *Sci. China Mater.* **63**, 2599–2605 (2020).
33. Nirmalkar, N., Pacek, A. W. & Barigou, M. Interpreting the interfacial and colloidal stability of bulk nanobubbles. *Soft Matter* **14**, 9643–9656 (2018).

Methods

Gold nanorods. Gold nanorods were synthesized according to a seed-mediated method developed by Ye et al.[34]. The TEM image and energy-dispersive spectra elemental mapping of original Au nanorods are shown in Supplementary Fig. 1. The concentration of Au nanorod aqueous solution used in the experiment was 50 µg ml^{-1}.

Ex situ experiment. To demonstrate the ability of O_2 to oxidize Au nanorods, 0.5 ml of Au nanorod solution was mixed with 0.5 ml of 1 M HBr and maintained at 70 °C with continuous bubbling of air. The control experiment was carried out under the same conditions but without additional air supply. The solution with bubbling air turned colourless within 5 min, which also suggests that O_2 can oxidize Au nanorods into colourless $AuBr_2-$ (ref. [27]). However, the colour of the solution without bubbling air was only slightly lighter after 20 min. Ex situ characterization of nanorods was carried out using Titan 80–300 and Themis, with the imaging corrector operated at 300 kV.

In situ TEM experiment. The reaction solution was first obtained by mixing (2:1 v/v) an Au nanorod aqueous solution with HBr solution (1 mM). A droplet of the reaction solution (~2 µl) was loaded onto an ultra-thin carbon film supported on a Cu frame (a TEM grid) and covered with another grid. Liquid pockets were well encapsulated between the two carbon films due to van der Waals forces after the evaporation of excessive liquid solution (Fig. 1a). Thus, a simple liquid cell was achieved with liquid pockets between two ultra-thin carbon films. The liquid cell was then loaded into an aberration-corrected transmission electron microscope for imaging. In situ experiments were carried out using a FEI Tecnai G20 operated at 200 kV. An incident electron dose rate of 200–800 e^{-2} s^{-1} was maintained for the study. We used Digital Micrograph to measure images.

EELS. EELS was carried out on a Tecnai F20 equipped with a monochromator operated at 200 kV. The sample was created using the same method as in the in situ experiment, except that the solution used here was pure water without HBr. The EELS spectrum of O_2 was obtained under TEM mode from the area that is constantly bubbling after being illuminated over an extended period of time (Fig. 1b and Supplementary Fig. 20). The EELS spectrum of water was collected immediately under electron beam illumination, and no nanobubble was generated during acquisition time. The EELS spectra from water without nanobubbles show an obvious peak at ~532 eV, consistent with O K-edge recorded from pure water[35,36]. However, EELS spectra from bubbling water not only show one peak at ~532 eV, but another at ~527 eV. The EELS spectra (Gatan EELS Atlas) from air containing a mixture of molecular oxygen and molecular nitrogen show the O K-edge at ~527 eV. Thus, the peak at ~527 eV recorded from bubbling water is the evidence required for production of molecular O_2. The slight shift of O K-edge from H_2O in water with nanobubbles was probably caused by the oxygen-containing groups (such as H_2O_2, $HO_2^{\bullet}$, $OH^{\bullet}$, O^- and so on) produced by irradiation of H_2O[37].

Computational models and methods. In our MD simulations the aqueous solution layer was ~10.0 × 10.0 × 16 nm^3, with 1,052 gas molecules (O_2) and the typical concentration of NaBr was 0.44 mol l^{-1} (~20% maximum saturation with 35,160 water molecules and 293 NaBr). Atoms on the (100) facet of the Au nanorod (face-centred cubic structure) were set fixed. The GROMO force field was used to describe interactions between different molecules. The extended simple point charge water model was used, and long-range electrostatic interaction was treated using the particle-mesh Ewald method with a real-space cut-off of 1.2 nm. The cut-off distance of the van der Waals interaction was also set at 1.2 nm. The simulation was performed in the canonical ensemble at 300 K for 10 ns, with ten ensemble simulations from different initial conditions being considered. Adsorbption time, T_A, refers to the diffusion time of O_2 molecules adsorbed on the Au nanorod surface in the MD simulation[38,39].

Electron dose and radiolysis product estimation. We first estimated the irradiation dose absorbed by water. The electron dose rate and steady-state concentration of radiolytic chemical species were calculated according to previous reports[30]. Grays per second (Gy s^{-1}), which is defined as the adsorption of one joule of energy per kilogram per second of water, was used as the unit for dose rate to describe the radiation effect of incident electrons on the thin liquid film:

$$\Phi = \frac{10^5 SI}{\pi a^2}\ (\text{Gy/s}) \qquad (\text{S1})$$

where S (MeV electron cm^2 g^{-1}) represents the stopping power in water, I (C s^{-1}) is the electron beam current and a (m) is the beam radius. The factor of 10^5 (m^2 electron Gy g^{-1} cm^{-2} MeV C) converts the units to Gy s^{-1}. The electron-stopping power of water is adopted from the ESTAR database, available from NIST[40]. Hence, dose rates in the in situ experiment with nanobubbles were 1.7×10^9 (Gy s^{-1}) and 9.2×10^8 (Gy s^{-1}). The corresponding steady-state concentration of H_2 and O_2 can be approximated using a power law:

$$C_{ss,i} \sim \alpha_i \Phi^{\beta_i} \qquad (\text{S2})$$

The calculated steady-state concentrations of H_2 and O_2 in the liquid cell at a dose rate of 1.7×10^9 Gy s^{-1} were 3.7 and 0.32 mM, respectively; the calculated steady-state concentrations of H_2 and O_2 in the liquid cell at a dose rate of 9.2×10^8 Gy s^{-1} were 2.7 and 0.21 mM, respectively.

According to previous calculations, the temperature changes in water caused by beam irradiation are only a few degrees Centigrade and the gases are more likely to have been formed by electrolysis of water molecules[30]. Calculations show that the level of H_2 is about one order of magnitude higher than that of O_2. The concentrations of saturated H_2 and O_2 in water were 0.8 mM (1 atm, 20 °C) and 0.255 mM (1 atm, 20 °C), respectively. Therefore, formation of oxygen nanobubbles is less likely so the majority of nanobubbles will be hydrogen, especially in the HBr solution, consistent with our experimental findings. We found that <10% of nanobubbles could accelerate local etching, even though they were very close to the nanorods.

Data availability

The data that support the findings of this study are available from the corresponding authors upon request.

References

34. Ye, X., Zheng, C., Chen, J., Gao, Y. & Murray, C. B. Using binary surfactant mixtures to simultaneously improve the dimensional tunability and monodispersity in the seeded growth of gold nanorods. *Nano Lett.* **13**, 765–771 (2013).
35. Jungjohann, K. L., Evans, J. E., Aguiar, J. A., Arslan, I. & Browning, N. D. Atomic-scale imaging and spectroscopy for in situ liquid scanning transmission electron microscopy. *Microsc. Microanal.* **18**, 621–627 (2012).
36. Aronova, M. A., Sousa, A. A. & Leapman, R. D. EELS characterization of radiolytic products in frozen samples. *Micron* **42**, 252–256 (2011).
37. Laffon, C., Lacombe, S., Bournel, F. & Parent, P. Radiation effects in water ice: a near-edge X-ray absorption fine structure study. *J. Chem. Phys.* **125**, 204714 (2006).
38. Aqvist, J. Ion-water interaction potentials derived from free energy perturbation simulations. *J. Phys. Chem.* **94**, 8021–8024 (1990).
39. Fang, G. & Chen, J. Hindered gas transport through an aqueous salt solution interface. *J. Phys. Chem. C Nanomater. Interfaces* **122**, 20774–20780 (2018).
40. Berger, M. J. et al. Stopping-power and range tables for electrons, protons, and helium ions. *NIST Physical Measurement Laboratory* https://doi.org/10.18434/T4NC7P (2017).

Acknowledgements

This work is especially for the 120th anniversary of Southeast University. We thank H. Zhang and H.-T. Zhang (SEU-FEI Nano-Pico Center, Southeast University) for support and useful discussions. The work at Lawrence Berkeley National Laboratory was supported by the US Department of Energy, Office of Science, Office of Basic Energy Sciences, Materials Sciences and Engineering Division under contract no. DE-AC02-05-CH11231 within the in situ TEM programme (no. KC22ZH). The work at Southeast University was supported by the National Natural Science Foundation of China (grant nos. 51420105003, 11327901, 61601116 and 61974021) and the National Science Fund for Distinguished Young Scholars (grant no. 11525415). J.C. thanks the Natural Science Foundation of Shanghai (grant no. 14ZR1448100, 19ZR1463200), and the Shanghai Supercomputer Center of China and Big Data Science Center of Shanghai Synchrotron Radiation Facility. W.W. thanks the China Scholarship Council (no. 201806090114) for financial support.

Author contributions

W.W., H.F., H.Z. and L.S. conceived and designed the experiments. W.W. and T.X. performed the experiments. J.C., H.M., J.Y. and H.F. developed the simulations. J.S., H.D. and Q.Z. participated in discussions and data analysis. Z.G. and T.B. synthesized samples. L.S. supervised the project and revised the paper with H.Z. and H.F. The manuscript contains contributions by all authors. All authors gave approval to the final version of the manuscript.

Competing interests

The authors declare no competing interests.

Additional information

Supplementary information The online version contains supplementary material available at https://doi.org/10.1038/s41563-022-01261-x.

Correspondence and requests for materials should be addressed to Haiping Fang, Haimei Zheng or Litao Sun.

Peer review information *Nature Materials* thanks Abhaya Datye and the other, anonymous, reviewer(s) for their contribution to the peer review of this work.

Reprints and permissions information is available at www.nature.com/reprints.